ACS APPLIED MATERIALS & INTERFACES

www.acsami.org

Research Article

Surface Coordination Environment Engineering on Pt_xCu_{1-x} Alloy Catalysts for the Efficient Photocatalytic Reduction of CO_2 to CH_4

Xin Wang, Haohong Liao, Wei Tan, Wang Song, Xue Li, Jiawei Ji, Xiaoqian Wei, Cong Wu, Chenxu Yin, Qing Tong, Bo Peng, Shangcong Sun, Haiqin Wan,* and Lin Dong

Cite This: *ACS Appl. Mater. Interfaces* 2024, 16, 22089−22101

Read Online

ACCESS | Metrics & More | Article Recommendations | Supporting Information

ABSTRACT: Alloy catalysts have been reported to be robust in catalyzing various heterogeneous reactions due to the synergistic effect between different metal atoms. In this work, aimed at understanding the effect of the coordination environment of surface atoms on the catalytic performance of alloy catalysts, a series of Pt_xCu_{1-x} alloy model catalysts supported on anatase-phase TiO_2 (Pt_xCu_{1-x}/Ti, x = 0.4, 0.5, 0.6, 0.8) were developed and applied in the classic photocatalytic CO_2 reduction reaction. According to the results of catalytic performance evaluation, it was found that the photocatalytic CO_2 reduction activity on Pt_xCu_{1-x}/Ti showed a volcanic change as a function of the Pt/Cu ratio, the highest CO_2 conversion was achieved on $Pt_{0.5}Cu_{0.5}$/Ti, with CH_4 as the main product. Further systematic characterizations and theoretical calculations revealed that the equimolar amounts of Pt and Cu in $Pt_{0.5}Cu_{0.5}$/Ti facilitated the generation of more Cu−Pt-paired sites (i.e., the higher coordination number of Pt−Cu), which would favor a bridge adsorption configuration of CO_2 and facilitate the electron transfer, thus resulting in the highest photocatalytic CO_2 reduction efficiency on $Pt_{0.5}Cu_{0.5}$/Ti. This work provided new insights into the design of excellent CO_2 reduction photocatalysts with high CH_4 selectivity from the perspective of surface coordination environment engineering on alloy catalysts.

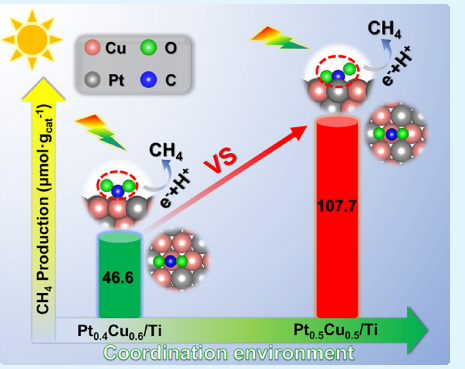

KEYWORDS: *Pt_xCu_{1-x} alloy, coordination environment, photocatalytic CO_2 reduction, Cu−Pt-paired sites, adsorption configuration*

1. INTRODUCTION

Solar-driven CO_2 reduction into hydrocarbon fuels has been considered as a promising approach to mitigating greenhouse effects and alleviating the depletion of fossil energy resources.[1−3] Among those products generated by photocatalytic reduction of CO_2 (e.g., CO, CH_3OH, CH_4, various multicarbon compounds, etc.), CH_4 could be used as an important clean fuel as well as an industrial feedstock for the production of carbon black, hydrogen, chloroform, and other high-value chemicals.[4−6] Although the reduction of CO_2 to CH_4 exhibits a great thermodynamic advantage in thermodynamics in comparison with the reduction of CO_2 to CO and CH_3OH in terms of reduction potentials, the kinetics of this process is extremely challenging due to the transfer of eight electrons and multiple protons.[7−9] Therefore, the generation of CH_4 during the photocatalytic reduction of CO_2 is always accompanied by the formation of undesired byproducts (e.g., CO and CH_3OH).[10] To address this dilemma, researchers have been devoted to designing efficient catalysts with high activity and CH_4 selectivity.[11,12]

Stable, inexpensive, and high-performance semiconductor catalysts are the foundation of photocatalytic carbon dioxide reduction reactions.[13−15] Anatase titanium dioxide (TiO_2) stands out among numerous semiconductor photocatalysts due to its excellent performance.[16,17] However, it has a relatively wide bandgap (3.2 eV), resulting in a narrow absorption spectrum and unexpected recombination of photogenerated charge carriers, which limited the photocatalytic efficiency. Various strategies were employed to enhance the photocatalytic performance of TiO_2 including cocatalyst deposition, semiconductor composites, surface sensitization of semiconductors, and ion doping.[18−20] Among them, cocatalyst deposition is an effective method to improve semiconductor performance, which not only significantly enhances the conductivity of the semiconductor and mitigates the recombination of charge carriers but also provides additional CO_2 adsorption and activation sites.[21,22]

Alloy nanocrystals are typical cocatalysts, which exhibit unique physicochemical properties.[23,24] Compared with monometallic nanocrystals, alloy nanocrystals performed better in the field of energy catalysis owing to the synergetic effects.[25]

Received: March 7, 2024
Revised: April 13, 2024
Accepted: April 16, 2024
Published: April 23, 2024

https://doi.org/10.1021/acsami.4c03861
ACS Appl. Mater. Interfaces 2024, 16, 22089−22101

Concretely, the incorporation of a second metal for the formation of bimetallic alloy can dramatically alter their electronic structures and atomic arrangement modes, further inducing the unprecedented improvement in performance.[26−28] For instance, Long et al. successfully synthesized Pd_xCu_1 alloys with different Pd/Cu ratios and loaded them onto TiO_2 nanosheets.[29] They found that the incorporation of trace Cu atoms in the Pd matrix can form the paired Cu−Pd sites for enhanced CO_2 adsorption and elevate the d-band center of Cu sites for improved CO_2 activation. Similarly, Wang et al. synthesized PtCu alloys with different Pt/Cu ratios and loaded them onto TiO_2.[30] They confirmed that PtCu alloys not only effectively promoted the separation and transfer of photogenerated charges but also facilitated the adsorption and activation of CO_2. Sooho Lee et al. reported that CuPt nanoclusters exhibited strong adsorption capability for CO_2 and intermediates, which contributed to an increased yield of CH_4.[31] In summary, the introduction of coalloy catalysts can broaden the light absorption spectrum of TiO_2 support and provide diverse adsorption and activation sites for CO_2, accordingly promoting the photocatalytic reduction of CO_2. Composition regulation of metal alloy is a strategy to design the catalysts with high active sites and the desired surface and thus reducing the recombination of charge carriers and enhancing the photocatalytic activity.[32−36] However, the impact of alloy coordination environments on the CO_2 adsorption mode at the atomic level is still ambiguous.

Herein, serious Pt_xCu_{1-x} alloys with different coordination environments were constructed as model cocatalysts to investigate this effect. To realize this target, we intentionally fixed their crystal structure and exposed (111) facet by Schlenk method under anhydrous and oxygen-free conditions. Subsequently, these particles were loaded onto TiO_2 to obtain a series of Pt_xCu_{1-x}/Ti catalysts. The roles of these cocatalysts on the catalytic activity and structure−activity relationship in photocatalytic CO_2 reduction were explored.

2. EXPERIMENTAL SECTION

2.1. Synthesis of Pt_xCu_{1-x}/TiO_2 Catalysts. *2.1.1. Synthesis of Pt_xCu_{1-x} Nano-Octahedrons.* Pt_xCu_{1-x} nano-octahedrons were synthesized according to the literature (Scheme 1 of the Supporting Information).[37] First, $Pt(acac)_2$ (x mmol), $Cu(acac)_2$ (1-x mmol), oleylamine (18.0 mL), and oleic acid (2.0 mL) were loaded into a three-necked flask (x = 0.4, 0.5, 0.6, 0.8), followed by degassing at 25 °C for 1 h under vigorous stirring (typically, >500 rpm). Then, the blue-green solution was heated to 130 °C under the protection of an argon stream. Afterward, tungsten hexacarbonyl ($W(CO)_6$, 100 mg) was added to the vigorously stirred solution, and the mixture was heated to 240 °C gradually and maintained for 40 min. After cooling to room temperature, the resulting mixture was transferred to a 50 mL centrifuge tube, subjected to four rounds of washing and centrifugation with a mixture of n-hexane and ethanol (in a ratio of 1:5). The expected product was Pt_xCu_{1-x} nano-octahedrons. Finally, the Pt_xCu_{1-x} nano-octahedrons were redispersed in n-hexane to form a nanoparticle suspension.

2.1.2. Preparation of Pt_xCu_{1-x}/Ti. Pt_xCu_{1-x}/Ti catalysts were prepared by a modified wetness impregnation method in a rotary evaporator (Scheme 1 of the Supporting Information). Anatase-phase TiO_2 after the precalcination at 450 °C for 2 h was used as the support. After the TiO_2 support and nanoparticle suspension were added into the rotary evaporator, vacuum drying was performed for 8 h to remove excess solution. The obtained powder was then transferred to a tube furnace, followed by calcination in a 7% H_2/Ar atmosphere at 200 °C for 2 h, with a ramp rate of 10 °C·min^{-1}. For convenience, the obtained catalysts were denoted as Pt_xCu_{1-x}/Ti (x = 0.4, 0.5, 0.6, 0.8.). Cu/Ti and Pt/Ti catalysts used as references were prepared in the same way as for Pt_xCu_{1-x}/Ti catalysts.

2.2. Characterizations. TEM and HRTEM images were captured on a JEM-2100 electron microscope instrument with an accelerating voltage of 200 kV. HAADF-STEM and EDS mapping were collected on a Thermo Fisher Scientific (FEI) Talos F200s electron microscope instrument.

X-Ray diffraction (XRD) patterns were obtained via a Philips X'Pert Pro diffractometer with nickel-filtered Cu Kα radiation (λ = 0.15 nm). The X-ray tube was operated at 40 kV and 40 mA.

The Brunauer−Emmet−Teller (BET) surface area was measured by N_2-physisorption at 77 K on a Micrometrics ASAP-2020 adsorption instrument. Before each measurement, the loaded sample (ca. 100 mg) was degassed in N_2/He at 300 °C for 3 h.

Inductively coupled plasma optical emission spectroscopy (ICP-OES) was performed by an Analytik Jena novAA 350/ZEEnit 650 P (Analytik Jena).

X-Ray photoelectron spectroscopy (XPS) analysis was performed on a PHI5000 Versa Probe high-performance electron spectrometer using monochromatic Al Kα radiation (1486.6 eV). Prior to the test, samples were evacuated in an ultrahigh vacuum (UHV) chamber at room temperature (pressure $<5 \times 10^{-7}$ Pa). The charging effect of the sample was compensated by calibrating all of the binding energies with the adventitious C 1s peak at 284.6 eV.

UV−vis diffuse reflectance spectroscopy (UV−vis DRS) experiment was conducted on a Shimadzu UV-2401 spectrophotometer, and the spectra were collected with a range of 200−800 nm, using $BaSO_4$ as the reference material.

Electron spin resonance (ESR) signals were collected at 77 K by an ESR JES FA200 spectrometer (JEOL) under xenon lamp illumination, and *in situ* ESR testing of the CO_2 radicals was performed using the spin trapping agent DMPO (5,5-dimethyl-1-pyrroline N-oxide).

Raman spectra were obtained via a LabRAM Aramis instrument at an excitation wavelength of 532 nm.

Electrochemical impedance spectroscopy (EIS) and photocurrent testing were carried out on a CHI 660 electrochemical workstation from Shanghai Chenhua Instrument Co., Ltd.

Photoluminescence (PL) spectra were collected on an F-7000 fluorescence spectrophotometer (Hitachi, Tokyo, Japan) with an excitation wavelength of 380 nm. The sample was in the form of a solid powder, and the slit width used for all tests was 1.5 nm.

The ^{13}C isotope tracer experiments were conducted on a Shimadzu 2020 GC-MS, with a m/z collection range of 10−200.

CO_2 temperature-programmed desorption (CO_2-TPD) experiments were conducted on a multifunctional chemical adsorption analyzer (Tianjin Pengxiang, China). The instrument was equipped with a quartz U-shaped tube reactor, and desorption was detected by a thermal conductivity detector (TCD). Each sample (100 mg) was pretreated by heating at a rate of 10 °C·min^{-1} under a flow of ultrahigh-purity He (30 mL·min^{-1}) up to 200 °C. After pretreatment, the sample was cooled to room temperature and exposed to a CO_2 flow (50 mL·min^{-1}) through the catalyst bed for 30 min, followed by purging with He flow (50 mL·min^{-1}) for 60 min. Subsequently, the sample will be heated to 500 °C at a heating rate of 10 °C·min^{-1}, and the programmed temperature desorption analysis will be conducted under a flow of He gas (30 mL·min^{-1}).

In situ diffuse reflectance infrared Fourier-transform spectroscopy (DRIFTS) experiments were conducted on a Nicolet 5700 FTIR spectrometer equipped with a high-sensitivity mercury cadmium telluride (MCT) detector cooled by liquid nitrogen. The range of the collected spectra was 1100−4000 cm^{-1}, with a resolution of 4 cm^{-1} (scan number = 32). The *in situ* cell (Harrick) was equipped with a ZnSe window and temperature control system. The catalyst powder placed on the sample holder was carefully flattened to enhance the intensity of the infrared reflection signal. The sample was purged with a He flow at 200 °C to remove physically adsorbed water and other impurities. After pretreatment, the sample was cooled to room temperature and the background spectrum was collected. Then, a mixture of CO_2 and water vapor (generated by bubbling N_2) was introduced into the *in situ* cell, and spectra were collected every 5 min

https://doi.org/10.1021/acsami.4c03861
ACS Appl. Mater. Interfaces 2024, 16, 22089−22101

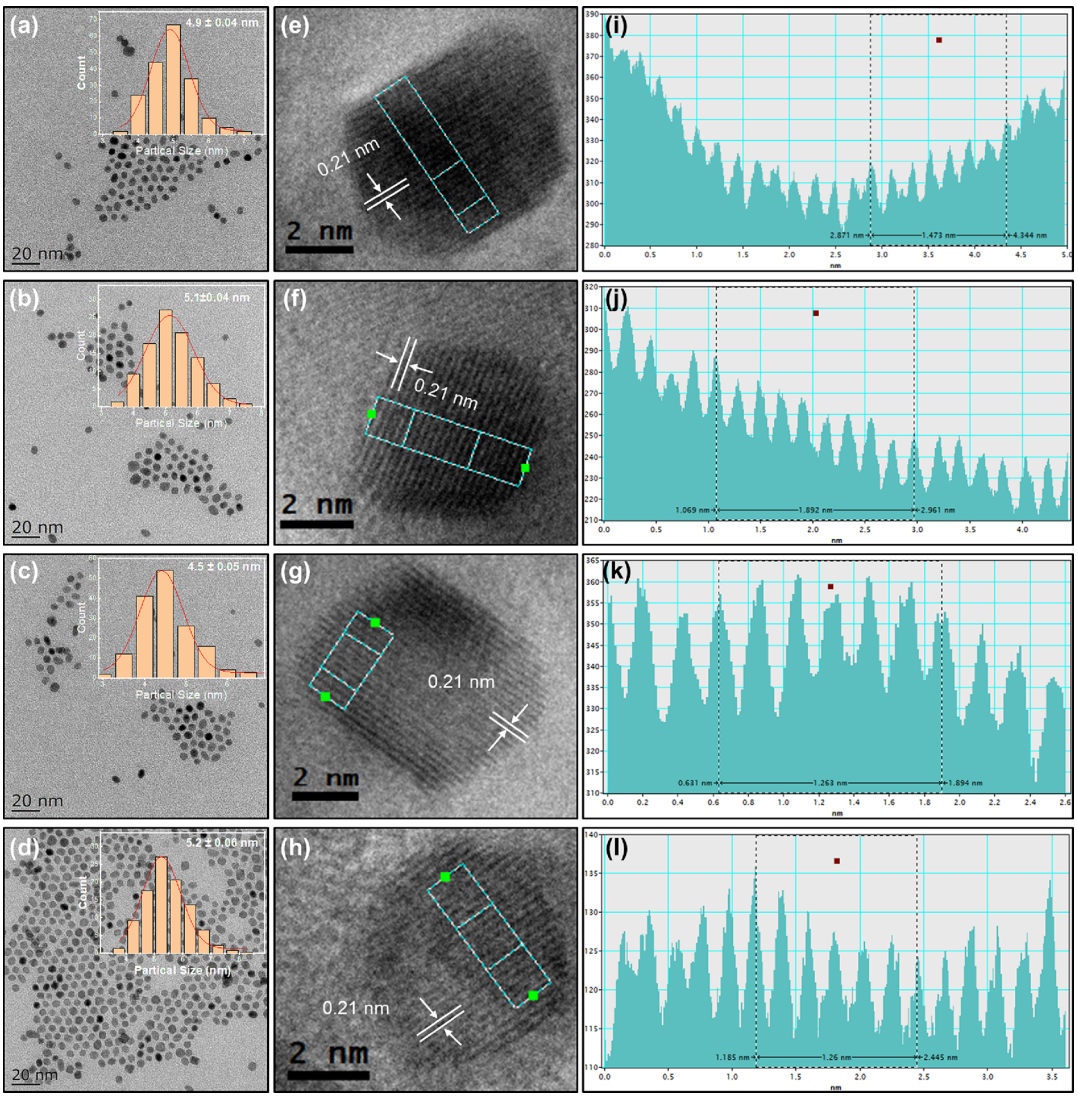

Figure 1. TEM images of Pt_xCu_{1-x} and Pt_xCu_{1-x}/Ti. Panels a–d represent the morphology and particle size distribution of Pt_xCu_{1-x}, panels e–h show the HRTEM images of Pt_xCu_{1-x}/Ti, and panels i–l represent the line profiles.

until adsorption saturation, with a total duration of exposure to the gas mixture of 300 W xenon lamp irradiation.

2.3. Photocatalytic CO_2 Reduction Experiments. The CO_2 photocatalytic reduction reaction was conducted under illumination from a 300W xenon lamp using a 100 mL stainless steel high-pressure reactor with a quartz window at the top. The catalyst (20 mg) was dispersed in 1 mL of H_2O, and the resulting suspension was dispersed on a quartz sand plate. High-purity CO_2 (0.2 MPa) was then introduced into the reactor, followed by full-spectrum illumination for 8 h. The generated CO and CH_4 were detected through gas chromatograph (GC). In the cycling test, the duration of each cycle was 8 h. After each cycle, the used catalysts were washed three times with distilled water, followed by drying in a vacuum oven at 80 °C. As for the stability test, the catalysts were exposed to the feeding flow for 24 h without any washing or drying/calcination, and the concentration of the generated CH_4 and CO was measured every 2 h.

The CO/CH_4 production and CH_4 selectivity were calculated by the following equations:

$$P = \frac{A_{sample} C_{standard} PV}{A_{standard} RTm} \quad (1)$$

$$S_{CO} = \frac{2n_{CO}}{2n_{CO} + 8n_{CH4}} \times 100\% \quad (2)$$

where A_{sample} is the CO/CH_4 peak area, $A_{standard}$ is the CO/CH_4 standard area, $C_{standard}$ is the concentration of CO/CH_4 standard gas, P is the pressure in the reactor, V is the reactor volume, R is the universal gas constant, T is the reactor temperature, and m is the catalyst weight.

2.4. Density Functional Theory Calculations. All density functional theory (DFT) calculations were performed with the Vienna Ab initio Simulation Package (VASP). The projector augmented-wave (PAW) method was carried out along with the generalized gradient approximation (GGA) and the Perdew–Burke–Ernzerhof (PBE) exchange-correlation functional. A plane wave energy cutoff of 450 eV was used, and the calculations were carried out by using the Gamma-point method for Brillouin zone sampling with a k-point grid of 1 × 1 × 1. The convergence criteria for energy and forces were set to 5×10^{-6} eV/atom and −0.03 eV/Å, respectively. Different compositions of Pt_xCu_{1-x} alloys, namely, $Pt_{0.4}Cu_{0.6}$, $Pt_{0.5}Cu_{0.5}$, and $Pt_{0.8}Cu_{0.2}$, were generated using the enumeration method implemented in the open-source code pymatgen. The adsorption energies of CO_2 on the alloy surfaces with different coordination environments were calculated along with the corresponding charge density difference. The adsorption energy (E_{ad}) was determined using the following formula: $E_{ad} = E_{tol} - E_{CO2} - E_{sur}$, where E_{tol} represents the total energy of CO_2 adsorbed on the alloy surface, E_{CO2} is the energy of the isolated CO_2 molecule, and E_{sur} is the energy of the alloy surface. Furthermore, the Gibbs free energy for the reduction of CO_2 to CH_4 on the surfaces of Pt_xCu_{1-x} alloys with varying compositions was calculated. The calculations of

https://doi.org/10.1021/acsami.4c03861
ACS Appl. Mater. Interfaces 2024, 16, 22089–22101

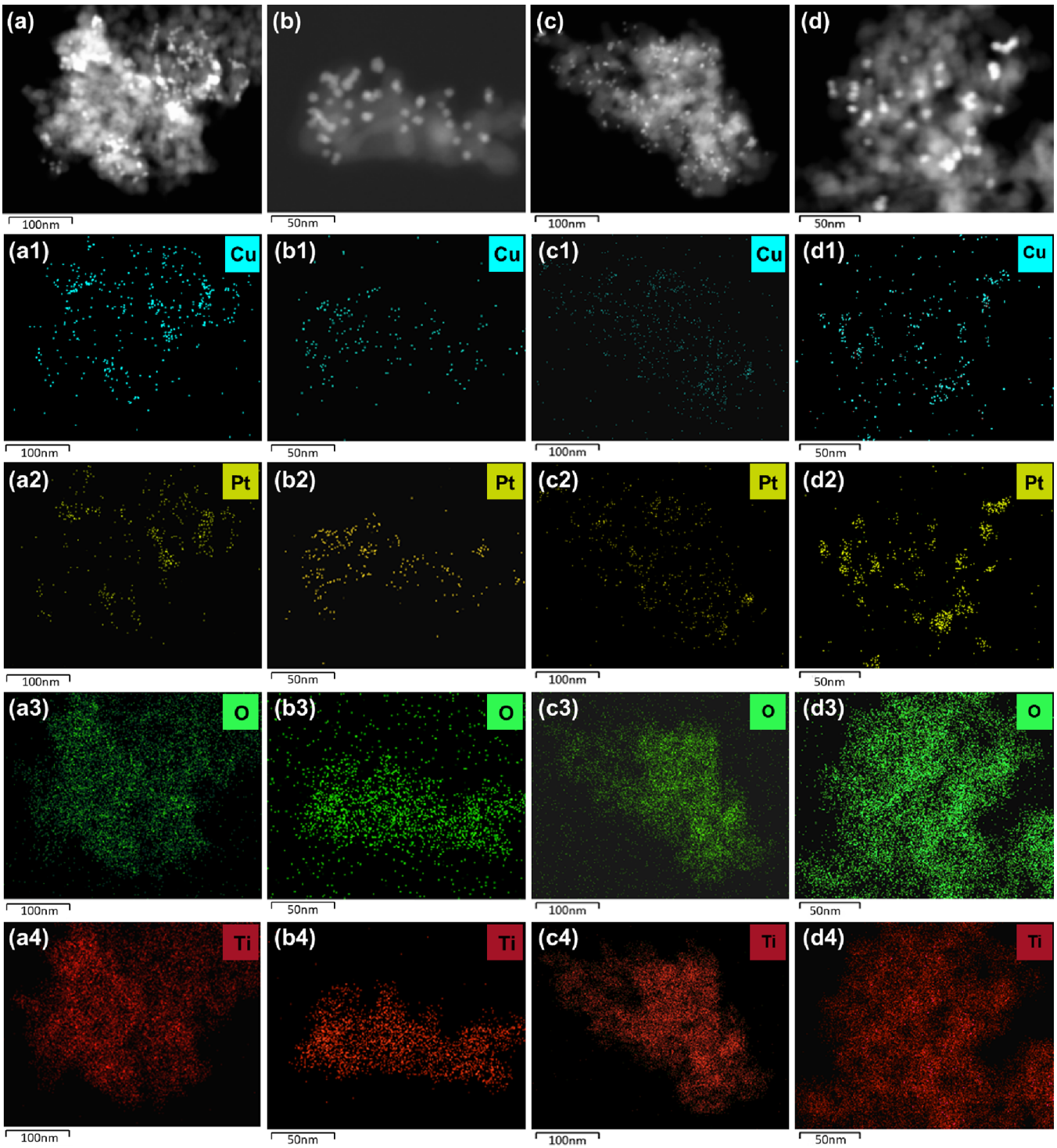

Figure 2. HAADF-STEM image (a−d) and EDS mapping (a1−a4, b1−b4, c1−c4, and d1−d4) of Pt_xCu_{1-x}/Ti.

$\Delta G_{f(n)}$ involved the summation of $\Delta E_{tol(n)}$ and $\Delta G_{t(n)}$, where $\Delta G_{t(n)} = \Delta E_{zpe(n)} - T\Delta S_{(n)}$. Here, n represents the respective reaction step, while $\Delta E_{tol(n)}$, $\Delta E_{zpe(n)}$, and $\Delta S_{(n)}$ denote the DFT energy differences, zero-point energy correction differences, and entropy changes under standard conditions (T = 298 K), respectively.

3. RESULTS AND DISCUSSION

3.1. Morphology and Textural Properties. The morphologies and particle size of Pt_xCu_{1-x} for samples were measured by TEM, and the results are shown in Figure 1. Pt_xCu_{1-x} particles are relatively uniform, with similar sizes around 5 nm, regardless of the Pt/Cu ratio. After being loaded onto TiO_2, all Pt_xCu_{1-x} alloy nanoparticles still maintain similar sizes (Figure S1). Furthermore, high-resolution TEM images reveal octahedral outlines (determined by line profiles) for all four samples, with lattice fringes spaced at 0.21 nm, corresponding to the (111) facets of the face-centered cubic Pt_xCu_{1-x} alloy, suggesting that Pt_xCu_{1-x} alloy nanoparticles had similar sizes and exposed the same crystal facets. X-Ray diffraction (XRD) testing was conducted to further confirm the crystal structure of the catalysts. As shown in Figure S2, all

https://doi.org/10.1021/acsami.4c03861
ACS Appl. Mater. Interfaces 2024, 16, 22089−22101

Table 1. Textural Properties, Element Content, Surface Atomic Concentration, and Pt_xCu_{1-x} Nanoparticle Average Particle Size of Samples

sample	surface area ($m^2 \cdot g^{-1}$)[aa]	pore volume ($cm^3 \cdot g^{-1}$)[a]	Pt content (wt. %)[b]	Cu content (wt. %)[b]	Pt content (atomic %)[c]	Cu content (atomic %)[c]	particle size (nm)[d]
TiO_2	78.8	0.36					
$Pt_{0.4}Cu_{0.6}/Ti$	78.4	0.49	0.69	0.36	0.36	0.59	4.9
$Pt_{0.5}Cu_{0.5}/Ti$	79.7	0.47	0.76	0.25	0.39	0.41	5.1
$Pt_{0.6}Cu_{0.4}/Ti$	74.9	0.45	0.83	0.18	0.43	0.29	4.5
$Pt_{0.8}Cu_{0.2}/Ti$	75.4	0.44	0.92	0.10	0.48	0.13	5.2

[a]Surface area and pore volume were determined by N_2 physisorption results. [b]Bulk phase concentrations of Pt and Cu were determined by ICP-OES. [c]Surface atomic concentrations of Pt and Cu were calculated based on XPS. [d]The average particle size of Pt_xCu_{1-x} nanoparticles was calculated based on the statistics of particle distribution analysis on TEM.

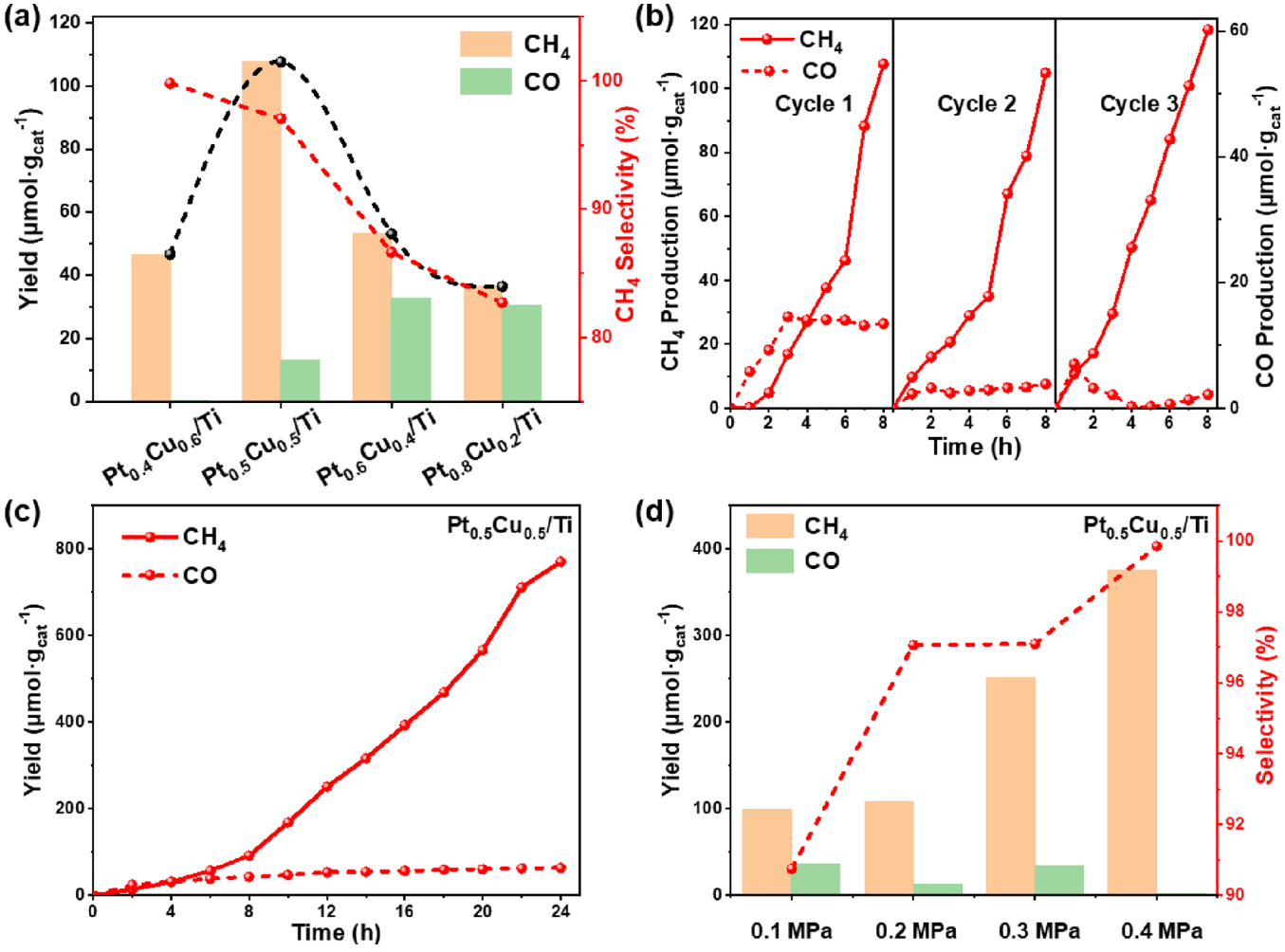

Figure 3. (a) CH_4 production, CO production, and CH_4 selectivity of Pt_xCu_{1-x}/Ti (reaction conditions: 0.2 MPa CO_2, 1 mL of H_2O, and 20 mg of catalyst); (b) cycle experiment test result of $Pt_{0.5}Cu_{0.5}/Ti$ (reaction conditions: 0.2 MPa CO_2, 1 mL of H_2O, and 20 mg of catalyst); (c) results of continuous 24 h CH_4 and CO production testing of $Pt_{0.5}Cu_{0.5}/Ti$ (reaction conditions: 0.2 MPa CO_2, 1 mL of H_2O, and 20 mg of catalyst); and (d) CH_4 production, CO production, and CH_4 selectivity of $Pt_{0.5}Cu_{0.5}/Ti$ under different pressures (reaction conditions: 1 mL of H_2O and 20 mg of catalyst).

samples exhibit the anatase phase of titanium dioxide, and no characteristic diffraction patterns for Pt_xCu_{1-x} were detected, indicating that Pt_xCu_{1-x} nanoparticles were highly dispersed on the TiO_2.[38]

In addition, HAADF-STEM and EDS mapping characterizations of Pt_xCu_{1-x}/Ti catalysts were collected. As shown in Figure 2, the blue color represents the Cu element, the yellow color represents the Pt element, the green color represents the O element, and the red color represents the Ti element, respectively. Both Cu and Pt are present in Pt_xCu_{1-x}/Ti and can be clearly distinguished. There is no particle agglomeration or element segregation observed in the Pt_xCu_{1-x} alloy across all samples, indicating that Pt_xCu_{1-x} nanoparticles were highly dispersed on the TiO_2. Additionally, the direct contact between Pt_xCu_{1-x} and TiO_2 can be observed, indicating that electrons can effectively transfer between the two materials.

The specific surface areas and contents of Pt and Cu of all samples were tested by N_2-sorption and ICP-OES. The results

https://doi.org/10.1021/acsami.4c03861
ACS Appl. Mater. Interfaces 2024, 16, 22089−22101

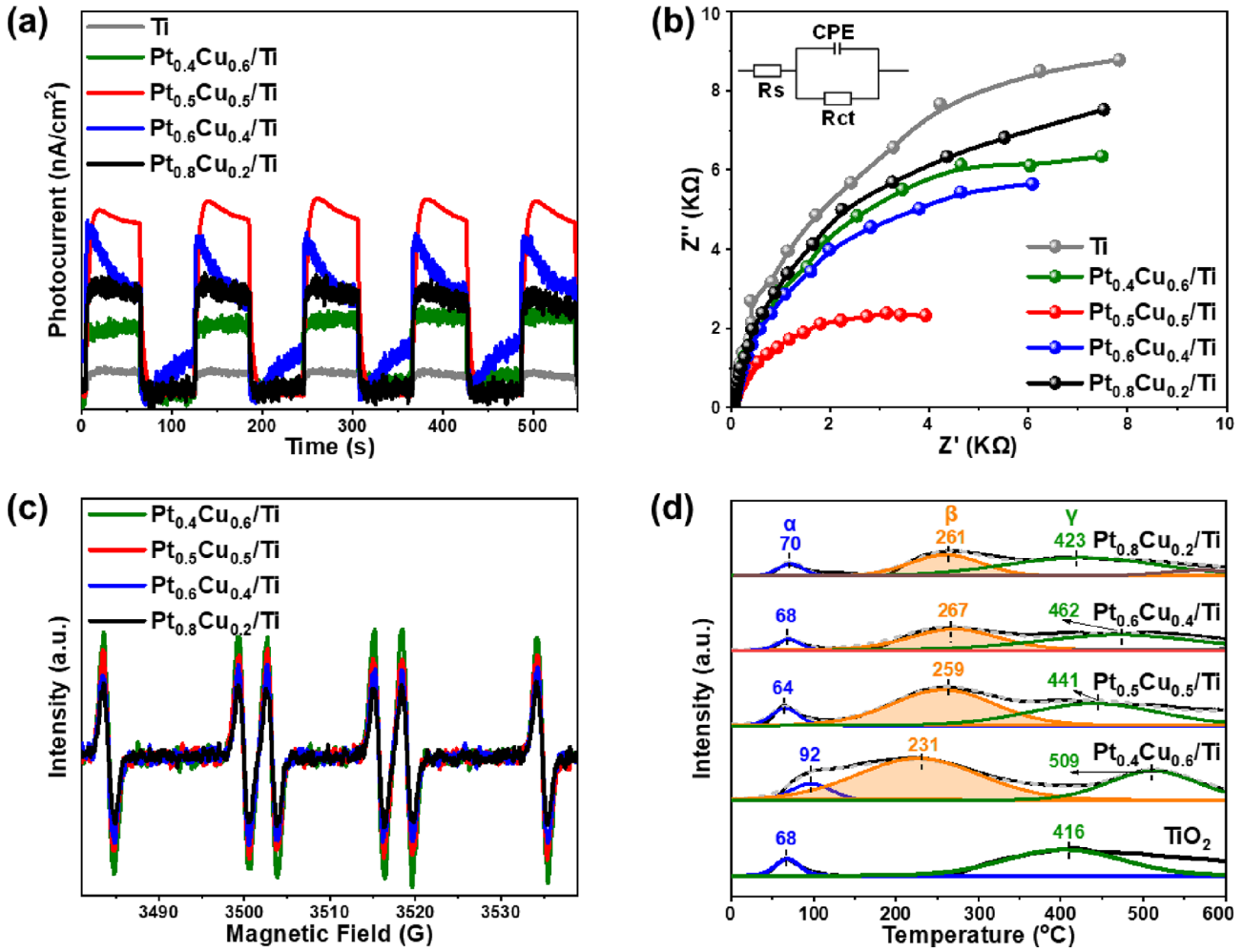

Figure 4. (a) Photocurrent responses and (b) electrochemical impedance spectroscopy curves of TiO_2 and Pt_xCu_{1-x}/Ti under UV−vis illumination; (c) ESR of Pt_xCu_{1-x}/Ti; (d) CO_2-TPD profiles of TiO_2 and Pt_xCu_{1-x}/Ti.

are presented in Figure S3 and listed in Table 1. It can be found that the surface areas and total pore volumes are similar for all samples. From the ICP results, the actual contents of Pt and Cu are close to the theoretical values, indicating that the Pt/Cu ratios were successfully controlled. It should be noted that the Pt/Cu content in the Pt_xCu_{1-x} alloy can be controlled within a certain range with a maximum value of 60%. Once beyond this range, the sample morphology becomes unstable (Figure S4). To further confirm the chemical valence of Pt, Cu, and Ti in all samples, X-ray photoelectron spectroscopy (XPS) experiments were carried out, and the results are presented in Figure S5. Pt and Cu elements in the samples were primarily present in zero valence, while Ti was predominantly Ti^{4+}. To better investigate the electron transfer between TiO_2 and Pt_xCu_{1-x}, Ti 2p XPS of TiO_2 has been measured. As shown in Figure S5, compared to TiO_2, the binding energy of Ti 2p in Pt_xCu_{1-x}/Ti shifts toward higher binding energies. This phenomenon indicate that electrons were transferred from TiO_2 to the Pt_xCu_{1-x} alloy, which further support the conclusion from EDS mapping that electrons can effectively transfer between TiO_2 to the Pt_xCu_{1-x} alloy. Furthermore, the quantitative results indicated that the surface atomic concentrations of Pt and Cu were consistent with their bulk concentrations, suggesting a uniform dispersion of Pt and Cu without segregation or phase separation.

3.2. Performance Evaluation for Photocatalytic Reduction of CO_2. Photocatalytic CO_2 reduction activity over Pt_xCu_{1-x}/Ti catalysts was evaluated, and the results are shown in Figure 3 and Figure S6. CH_4 and CO were detected over all catalysts (Figure S6), suggesting that CH_4 and CO were the main products of photocatalytic CO_2 reduction on Pt_xCu_{1-x}/Ti catalysts (Figure S8a). By supporting Cu, Pt_xCu_{1-x}, and Pt nanoparticles on TiO_2, the photocatalytic activity was significantly enhanced, indicating the contribution of the cocatalysts to the reaction activity. The photocatalytic activities of Pt_xCu_{1-x}/Ti have been obviously enhanced compared with loading Cu and Pt nanoparticles separately, which confirmed the synergy for alloying catalysts (Figure 3a). It is worth noting that, at the same loading amount, the CH_4 production showed a close correlation with the chemical composition of Pt_xCu_{1-x}. As the Pt content increased, the CH_4 production increased significantly, while the CH_4 production gradually decreased with a further increase in the Pt content. However, the CH_4 selectivity still decreased monotonically with an increasing Pt content. Cycle experiments were performed on the $Pt_{0.5}Cu_{0.5}$/Ti catalyst, as shown in Figure 3b. After three cycles, $Pt_{0.5}Cu_{0.5}$/Ti still kept excellent photocatalytic CO_2 reduction activity. It also maintained high activity in continuous 24 h durability testing (Figure 3c), indicating good stability of the catalyst. ^{13}C isotopic tracer experiments can provide a direct proof of the carbon

https://doi.org/10.1021/acsami.4c03861
ACS Appl. Mater. Interfaces 2024, 16, 22089−22101

source. To validate the origin of produced CO and CH_4, ^{13}C isotope labeling experiments were conducted with $^{13}CO_2$ used as a gas source. As shown in Figure S7, the m/z values of the detected products were 17 ($^{13}CH_4$) and 29 (^{13}CO), indicating that all the CH_4 and CO produced in the system come from the reduction of CO_2.[39,40] Moreover, the catalytic activity of the $Pt_{0.5}Cu_{0.5}$/Ti catalyst was tested under different pressures, with the other reaction conditions remaining the same as described above (Figure 3d). The results revealed that both the reaction activity and CH_4 selectivity increased as the pressure was raised. It is noteworthy that CH_4 exhibited an activity of 99.3 μmol·g^{-1} at atmospheric pressure, indicating the promising potential of this catalyst for industrial applications. The photocatalytic performance of $Pt_{0.5}Cu_{0.5}$/Ti is more excellent than that of other related photocatalysts in the literature (summarized in Table S1). Moreover, external quantum efficiency (EQE) is considered a significant intrinsic parameter for evaluating the photon-to-product efficiency of a photocatalytic system. Therefore, the EQE of $Pt_{0.5}Cu_{0.5}$/Ti was tested. As shown in Table S2, the external EQE of $Pt_{0.5}Cu_{0.5}$/Ti is quite low, with values of only 0.018, 0.00014, 0.00015, and 0.00012% at wavelengths of 325, 420, 450, and 475 nm, respectively. According to previous reports, achieving high EQE is challenging as it is limited by multiple factors in a photocatalytic system, including multi-electron transfer steps in reaction, catalytic performance of the catalyst, photophysical properties of the photosensitizer, and, importantly, electron transfer between the photosensitizer and catalyst.[41] Here, $Pt_{0.5}Cu_{0.5}$/Ti exhibited high CH_4 and CO production. Therefore, it is reasonably concluded that the low quantum efficiency is due to the absence of a photosensitizer in our reaction system.

In general, H_2 evolution is a competing reaction in photocatalytic CO_2 reduction. However, no H_2 gas was detected in the gas-phase reaction products (Figure S8b), which may be because H atoms reacted with intermediate products to produce CH_4. Some oxidized products also may be produced as no hole quenchers were added during the photoreduction experiment.[42] As expected, O_2 was detected in the outlet gas (Figure S8b). It should come from the oxidization of H_2O because H_2O was used as the reductant (hydrogen source). So, O_2 was the oxidizing product during the photoreduction of CO_2. Additionally, liquid-phase reaction experiments were also conducted. Unfortunately, no liquid-phase products were detected by FID (Figure S8c). This phenomenon may be due to the competitive adsorption of H_2O and CO_2 in the liquid phase, and H_2O occupies the active site, resulting in the inability of CO_2 adsorption and activation.

3.3. Adsorption and Surface Reactivity Behavior. The surface structures affect the final photocatalytic activity. Therefore, the surface structures of the Pt_xCu_{1-x}/Ti samples were obtained via ATR-FTIR (Figure S9) and Raman spectroscopy for further verification (Figure S10). The results showed that all samples exhibited vibrational peaks corresponding to Ti−O and Ti−O−Ti bonds with nearly identical intensities; thus, the influence of TiO_2 surface structures on the activity was excluded.[43,44] Therefore, the enhancement of activity might be related to the cocatalysts rationally.

According to previous work, Pt_xCu_{1-x} nanoparticles bound to TiO_2 can act as cocatalysts to improve charge separation and provide active sites.[45−47] To investigate this promoting effect, a series of photoelectrochemical characterizations were conducted. The light absorption capabilities of the samples were measured by the UV−vis diffuse reflectance spectrum (Figure S11). TiO_2 exhibited light absorption in the ultraviolet region with an absorption edge occurring at around 390 nm. In comparison with TiO_2, Pt_xCu_{1-x}/Ti samples displayed broad background absorption in both visible and ultraviolet region, which could be attributed to that bound electrons absorbed by nonplasmonic Pt_xCu_{1-x} nanocrystals and excited to higher energy levels through interband transitions.[30,31,48] Photocurrent measurements were used to evaluate the separation efficiency of photogenerated electrons and holes; the larger photocurrent, the higher separation efficiency. Figure 4a exhibits that the addition of Pt_xCu_{1-x} nanoparticles significantly enhanced the photocurrent of TiO_2, suggesting the positive function of the cocatalyst in separating the photogenerated electron−hole pairs within the TiO_2 semiconductor.[49] Notably, $Pt_{0.5}Cu_{0.5}$/Ti exhibited the highest photocurrent intensity, indicating the highest efficiency of photogenerated electrons and holes in this sample.[50] Electrochemical impedance spectroscopy (EIS) and photoluminescence spectroscopy (PL) were further conducted to confirm this promoting effect, and the results are depicted in Figure 4b and Figures S12 and S13. As shown in Figure 4b, the Nyquist curve of $Pt_{0.5}Cu_{0.5}$/Ti exhibits the smallest arc radius, indicating the lowest charge transfer impedance and thus the fastest electron-transfer capability. The inset of Figure 4b displayed the equivalent circuit (Randles model) that was used to fit Nyquist diagrams, with specific values of Rct and N provided in Figure S12. The value of Rct followed the sequence of $Pt_{0.5}Cu_{0.5}$/Ti (6.45 KΩ) < $Pt_{0.6}Cu_{0.4}$/Ti (12.85 KΩ) < $Pt_{0.4}Cu_{0.6}$/Ti (15.04 KΩ) < $Pt_{0.8}Cu_{0.2}$/Ti (19.78 KΩ) < Pt/Ti (21.13 KΩ), further supporting the viewpoint that $Pt_{0.5}Cu_{0.5}$/Ti with the fastest electron-transfer process on the electrode surface. The PL spectrum (Figure S13) of $Pt_{0.5}Cu_{0.5}$/Ti showed the weakest intensity of the photoluminescence peak, indicating that the relative reduction of photogenerated electron−hole recombination in $Pt_{0.5}Cu_{0.5}$/Ti.[51,52] These results collectively indicated that $Pt_{0.5}Cu_{0.5}$/Ti had the highest ability for photogenerated charge transfer among all of the samples, which resulted in more photogenerated electrons available on the surface of $Pt_{0.5}Cu_{0.5}$/Ti. Therefore, the reduction of CO_2 is more favorable on $Pt_{0.5}Cu_{0.5}$/Ti, leading to an increased production of CH_4 (and CO).

To verify the above conjecture, *in situ* ESR and CO_2-TPD experiments were performed to test the CO_2 adsorption and activation abilities of different samples. *In situ* ESR was employed to detect the signal of DMPO-$\bullet CO_2^-$ in the presence of H_2O and DMPO. A higher intensity of the DMPO-$\bullet CO_2^-$ signal suggested the generation of more $\bullet CO_2^-$ radicals during the photocatalytic process.[53,54] From Figure S14, the intensity of $\bullet CO_2^-$ radicals enhanced with the illumination time increasing for all samples. It is noted that the $\bullet CO_2^-$ radicals showed a linear correlation with the Cu content in different samples, demonstrating that a higher Cu content resulted in more $\bullet CO_2^-$ radicals generation (Figure 4c and Figures S15 and S16).[55] Additionally, the adsorption of CO_2 by catalysts is an important part of the photocatalytic CO_2 reduction; thus, CO_2-TPD experiments were carried, and the corresponding peak areas were calculated in this study to further reveal the CO_2 adsorption capacity of Pt_xCu_{1-x}/Ti. As shown in Figure 4d, all samples exhibit peaks attributed to physical adsorption (α) and carbonate forms (γ) of CO_2 desorption, with nearly identical peak areas (Table S3). In addition to peaks attributed to physical adsorption (α) and carbonate form adsorption (γ) of CO_2 desorption, the Pt_xCu_{1-x}/Ti series of catalysts also exhibits a CO_2 desorption peak at 230−270 °C, which can be attributed to chemisorbed CO_2 desorption. When the Cu content decrease

https://doi.org/10.1021/acsami.4c03861
ACS Appl. Mater. Interfaces 2024, 16, 22089−22101

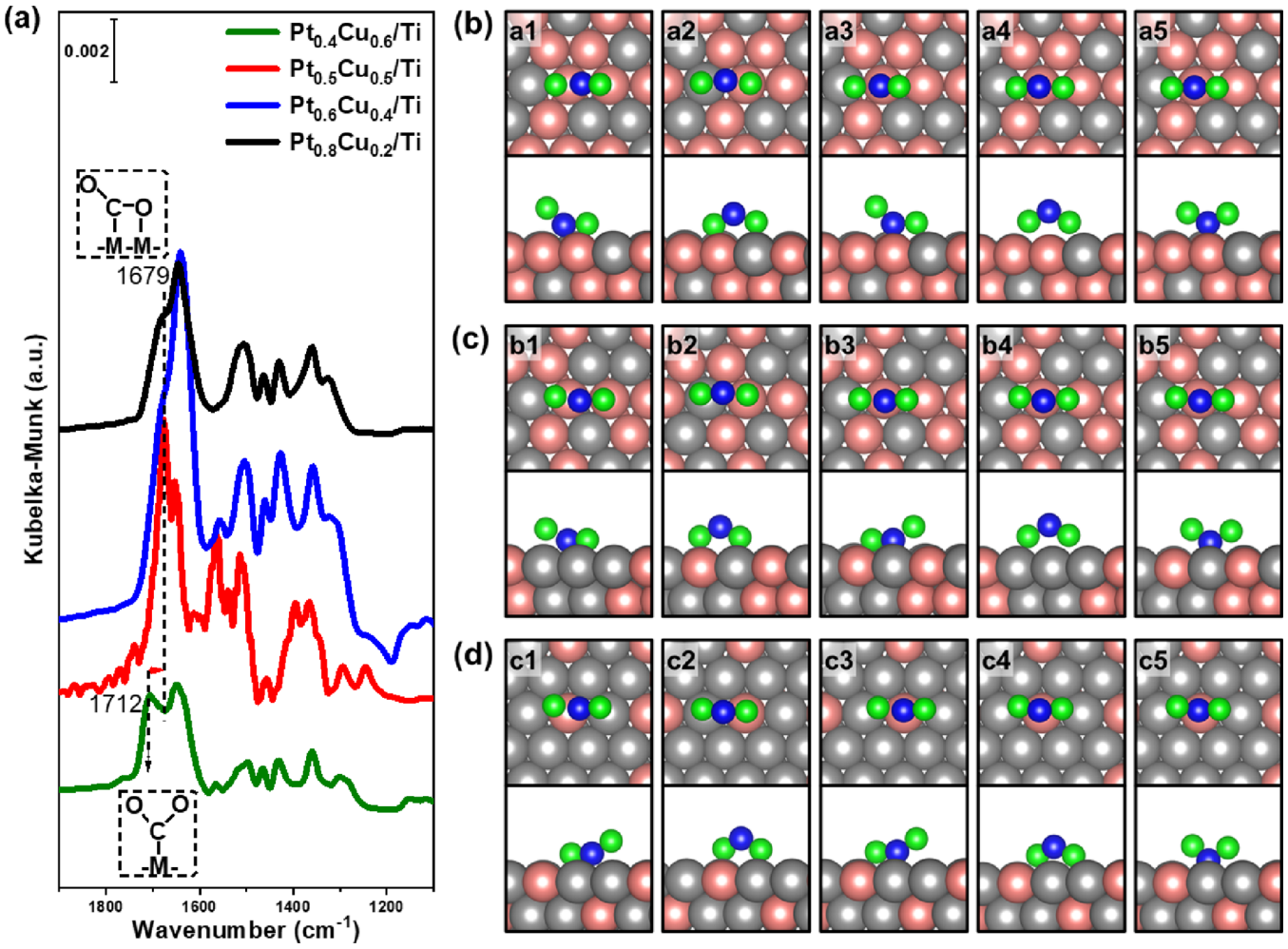

Figure 5. (a) *In situ* FTIR spectra of Pt_xCu_{1-x}/Ti after CO_2 adsorption saturation. CO_2 adsorption configurations on Pt_xCu_{1-x}/Ti. Panels b−d represent $Pt_{0.4}Cu_{0.6}$/Ti, $Pt_{0.5}Cu_{0.5}$/Ti, and $Pt_{0.8}Cu_{0.2}$/Ti, respectively. panels b1, c1, and d1 represent O-M-C; panels b2, c2, and d2 represent O-M-M-O; panels b3, c3, and d3 represent O-M-M-C; panels b4, c4, and d4 represent O-M-O; and panels b5, c5, and d5 represent M-C. Gray, red-brown, green, and blue balls represent Pt, Cu, O, and C atoms, respectively.

from 0.6 to 0.2 wt.%, a gradual reduction in the desorption peak attributed to chemisorbed CO_2 (peak β), indicating that Cu favors the adsorption of CO_2, which was also well supported by EPR results (Figure S5). It is noteworthy that, as the Cu content decreases from 0.6 to 0.5 wt.%, the peak β shifts to higher temperatures, indicating stronger chemisorption of CO_2, suggesting that $Pt_{0.4}Cu_{0.6}$/Ti and $Pt_{0.5}Cu_{0.5}$/Ti potentially exhibit different CO_2 adsorption modes. Further reduction in Cu content results in almost no change in the desorption temperature corresponding to peak β, indicating consistent CO_2 adsorption modes for $Pt_{0.5}Cu_{0.5}$/Ti, $Pt_{0.6}Cu_{0.4}$/Ti, and $Pt_{0.8}Cu_{0.2}$/Ti. Based on the characterization results mentioned above, it can be inferred that Cu sites favor CO_2 adsorption, and $Pt_{0.4}Cu_{0.6}$/Ti exhibits potentially a different CO_2 adsorption mode compared to the other three samples.[56,57]

To validate this hypothesis, we investigated the adsorption behavior of CO_2 on Pt_xCu_{1-x} surfaces by *in situ* DRIFTS. Figure 5a presents the CO_2 adsorption spectra of Pt_xCu_{1-x}/Ti. A broad band emerged at around 1679 cm^{-1} for $Pt_{0.4}Cu_{0.6}$/Ti, $Pt_{0.5}Cu_{0.5}$/Ti, $Pt_{0.6}Cu_{0.4}$/Ti, and $Pt_{0.8}Cu_{0.2}$/Ti, which was corresponded to the stretching vibration of the C═O bond in CO_2. However, the band of $Pt_{0.4}Cu_{0.6}$/Ti showed a significant blueshift to approximately 1712 cm^{-1}. Considering that the peak wavelength appears to blue-shift as the vibrational frequency increases, it could be deduced that the CO_2 adsorption mode on $Pt_{0.4}Cu_{0.6}$/Ti was different from that on the other Pt_xCu_{1-x}/Ti samples. Generally, there are five possible adsorption configurations of CO_2 on metal surfaces, as depicted in Figure 5b−d. For brevity, they were labeled as O-M-C, O-M-M-O, O-M-M-C, O-M-O, and M-C.[58] O-M-C, O-M-O, and M-C represent CO_2 molecules adsorbed on a single Cu atom, while O-M-M-O and O-M-M-C represent CO_2 molecules adsorbed on a Cu−Pt atomic pairs. Therefore, the M-C, O-M-C, and O-M-O configurations have a larger CO_2 adsorption capacity than O-M-M-C and O-M-M-O. Given that the CO_2 desorption peak area of $Pt_{0.4}Cu_{0.6}$/Ti was much larger than that of the other three samples ($Pt_{0.5}Cu_{0.5}$/Ti, $Pt_{0.6}Cu_{0.4}$/Ti, and $Pt_{0.8}Cu_{0.2}$/Ti), the adsorption mode of CO_2 on $Pt_{0.4}Cu_{0.6}$/Ti surfaces might be one kind of M-C, O-M-C, or O-M-O, while on the surfaces of $Pt_{0.5}Cu_{0.5}$/Ti, $Pt_{0.6}Cu_{0.4}$/Ti, and $Pt_{0.8}Cu_{0.2}$/Ti, the adsorption mode may involve O-M-M-C or O-M-M-O configurations. This was consistent with the results of the CO_2-TPD experiments.

To further confirm the adsorption configurations of CO_2 on different samples, density functional theory (DFT) calculations based on the model above were conducted to measure the adsorption energies of five possible CO_2 adsorption modes.[58,59] Infrared spectra of $Pt_{0.6}Cu_{0.4}$/Ti and $Pt_{0.8}Cu_{0.2}$/Ti were similar; therefore, $Pt_{0.4}Cu_{0.6}$/Ti, $Pt_{0.5}Cu_{0.5}$/Ti, and $Pt_{0.8}Cu_{0.2}$/Ti were

https://doi.org/10.1021/acsami.4c03861
ACS Appl. Mater. Interfaces 2024, 16, 22089−22101

selected as representative samples. Based on TEM results, the Pt(111) surface of Pt with a face-centered cubic structure was considered. Furthermore, based on XPS results, Pt and Cu were uniformly dispersed. Thus, three models were constructed by randomly substituting Cu for Pt according to the atomic molar ratio, as shown in Figure S16. The adsorption energies of the five adsorption configurations were calculated for each sample (Figure 6). For $Pt_{0.4}Cu_{0.6}$/Ti, the adsorption energies of CO_2 for

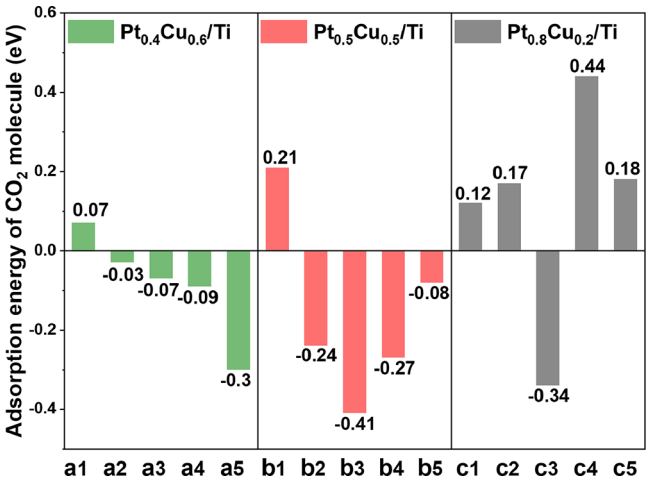

Figure 6. CO_2 adsorption energy of different configurations on $Pt_{0.4}Cu_{0.6}$/Ti, $Pt_{0.5}Cu_{0.5}$/Ti, and $Pt_{0.8}Cu_{0.2}$/Ti.

the five configurations were 0.07, −0.03, −0.07, −0.09, and −0.3 eV. Therefore, M-C adsorption mode is more likely to occur on the $Pt_{0.4}Cu_{0.6}$/Ti surface. Similarly, for $Pt_{0.5}Cu_{0.5}$/Ti, the adsorption energies of the five adsorption configurations were 0.21, −0.24, −0.41, −0.27, and −0.08 eV. While the adsorption energies of $Pt_{0.8}Cu_{0.2}$/Ti were 0.12, 0.17, −0.34, 0.44, and 0.18 eV. These results showed that adsorption for $Pt_{0.5}Cu_{0.5}$/Ti and $Pt_{0.8}Cu_{0.2}$/Ti occurred in the O-M-M-C form. Therefore, this confirmed that the CO_2 adsorption modes on Pt_xCu_{1-x}/Ti surfaces differ from each other and Cu−Pt atomic pairs were the most favorable active sites for capturing CO_2 and facilitating subsequent reduction reactions.

After the adsorption modes were identified, the role of the electronic structure in modulating catalytic activity was analyzed by charge density difference. As shown in Figure 7, the yellow

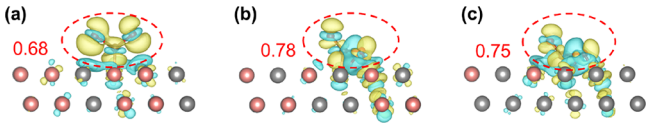

Figure 7. Charge density difference of (a) $Pt_{0.4}Cu_{0.6}$/Ti, (b) $Pt_{0.5}Cu_{0.5}$/Ti, and (c) $Pt_{0.8}Cu_{0.2}$/Ti.

regions represent charge accumulation, while the blue regions represent charge depletion. When CO_2 was adsorbed, electron transfer occurred between the pristine catalysts and CO_2 molecules. These electrons mainly originated from the photogenerated electrons formed in the TiO_2 semiconductor under photon excitation. Charge transfer occurred between $*CO_2$ and the catalyst through the O−Pt−Cu-C or Cu−C bonds, which was a crucial step in the evolution of $*CO_2$. During the activation process, $Pt_{0.5}Cu_{0.5}$ and $Pt_{0.8}Cu_{0.2}$ injected charges into the $*CO_2$ species more rapidly through the O−Pt−Cu−C bonds, leading to favorable charge transfer and distribution compared with $Pt_{0.4}Cu_{0.6}$ in the Cu−C mode. Additionally, Bader charge analysis revealed that CO_2 adsorbed on $Pt_{0.5}Cu_{0.5}$/Ti gained the largest amount of electrons, indicating that CO_2 is more easily activated, which facilitates the occurrence of photocatalytic CO_2 reduction reactions.[11] These findings are consistent with the results from photocurrent, EIS, and PL experiments.

3.4. Mechanism of Enhancing CH_4 Production via the Coordination Environment Engineering. To investigate the reasons for the differences in CH_4 selectivity on Pt_xCu_{1-x}/Ti catalysts, *in situ* diffuse reflectance infrared Fourier-transform spectroscopy (DRIFTS) was conducted, and the results are shown in Figure 8. After saturation with H_2O and CO_2, the sample surfaces were irradiated with a 300 W xenon lamp. Significant differences occurred in the spectra among the samples in the range of 1100−1800 cm^{-1}. After adsorption saturation, a band at 1712 cm^{-1}, which is attributed to $*CO_2$ species adsorbed in the M-C configuration, was detected on $Pt_{0.4}Cu_{0.6}$/Ti (Figure 8a).[60−62] After 12 min of illumination, bands corresponding to *COOH appeared near 1749 and 1571 cm^{-1}.[62,63] At the same time, the band attributed to H_2O at 1648 cm^{-1} was significantly consumed, indicating that the photocatalytic CO_2 reduction reaction was driven.[48,64] Subsequently, a new band assigned to *CHO species appeared at 1688 cm^{-1} and a band attributed to *CO was detected at 1359 cm^{-1}.[65] As the illumination time increased, vibration bands attributed to $*CH_2$ and $*CH_3$ appeared at 1470 and 1397 cm^{-1}, respectively.[48] But no band attributed to $*CH_2O$ and $*CH_3O$ was observed, which might be two important intermediates in the "formaldehyde" pathway. Therefore, it is inferred that the reaction may undergo the following mechanism on $Pt_{0.4}Cu_{0.6}$/Ti: $*CO_2 \rightarrow *COOH \rightarrow *CO \rightarrow *CHO \rightarrow *C \rightarrow *CH \rightarrow *CH_2 \rightarrow *CH_3 \rightarrow CH_4$.

Due to the difference in adsorption configuration of CO_2, the spectra of the $Pt_{0.5}Cu_{0.5}$/Ti and $Pt_{0.8}Cu_{0.2}$/Ti exhibited significant discrepancy with that on $Pt_{0.4}Cu_{0.6}$/Ti. Specifically, $Pt_{0.5}Cu_{0.5}$/Ti and $Pt_{0.8}Cu_{0.2}$/Ti possessed several identical bands during the light on process, but the changes were more significant for $Pt_{0.5}Cu_{0.5}$/Ti. For $Pt_{0.5}Cu_{0.5}$/Ti (Figure 8b), the band at 1677 cm^{-1} was attributed to $*CO_2$ adsorbed on the Cu−Pt atomic pairs, and it attenuated with increasing illumination time, indicating photocatalytic CO_2 conversion on the surface.[60] It is worth mentioning that, after 12 min of illumination, new bands appeared at 1725 and 1571 cm^{-1}, attributed to *COOH species, indicating the formation of *COOH intermediates.[66,67] At the same time, the intensity of the band attributed to H_2O at 1649 cm^{-1} significantly decreased, indicating the occurrence of the photocatalytic CO_2 reduction reaction.[48,64] Subsequently, a band assigned to *CO emerged near 1361 cm^{-1}, followed by two bands assigned to *CHO and $*CH_2O$ at 1610 and 1508 cm^{-1}, respectively.[63,68] As the illumination time further increased, the bands attributed to $*CH_3O$ gradually appeared at 1128 and 1463 cm^{-1}.[62,69] Based on the phenomena observations from *in situ* DRIFTS, it can be concluded that the adsorption of CO_2 on Cu−Pt atomic pairs in the O-M-M-C configuration significantly enhances the formation of $*CH_2O$ and $*CH_3O$ species, which are crucial intermediates. Furthermore, based on the sequence of intermediate species generation, it is speculated that the reaction mechanism occurred as follows: $*CO_2 \rightarrow *COOH \rightarrow *CO \rightarrow *CHO \rightarrow *CH_2O \rightarrow *CH_3O \rightarrow CH_4 + *O \rightarrow CH_4 + *OH \rightarrow CH_4 + H_2O$. Whereas for the spectra of $Pt_{0.8}Cu_{0.2}$/Ti (Figure 8c), all the bands during adsorption and reaction process showed subtle

https://doi.org/10.1021/acsami.4c03861
ACS Appl. Mater. Interfaces 2024, 16, 22089−22101

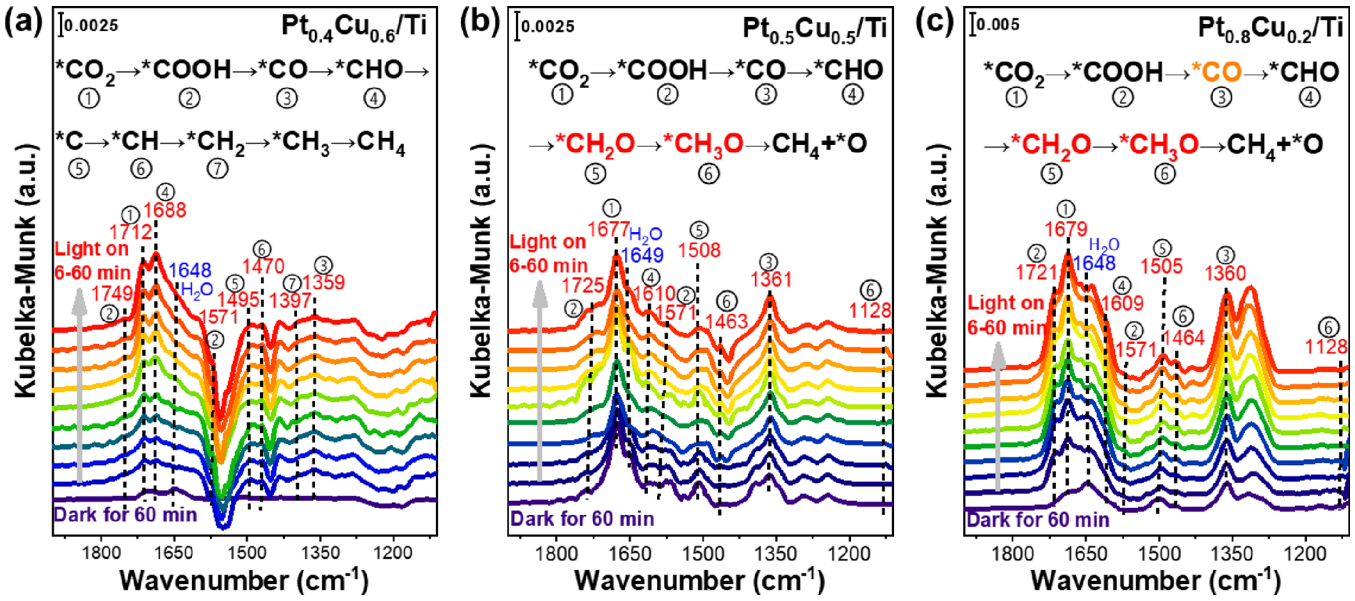

Figure 8. *In situ* DRIFTS of CO_2 reacted with preadsorbed H_2O on (a) $Pt_{0.4}Cu_{0.6}$/Ti, (b) $Pt_{0.5}Cu_{0.5}$/Ti, and (c) $Pt_{0.8}Cu_{0.2}$/Ti at room temperature.

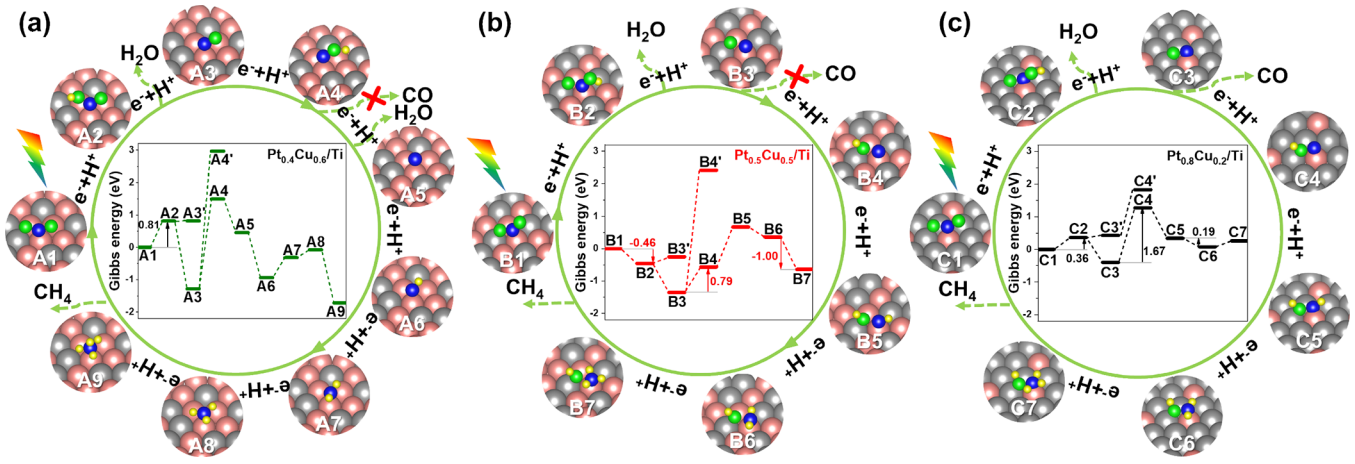

Figure 9. Proposed reaction paths on (a) $Pt_{0.4}Cu_{0.6}$/Ti, (b) $Pt_{0.5}Cu_{0.5}$/Ti, and (c) $Pt_{0.8}Cu_{0.2}$/Ti.

changes, and the production of *CO dominated, which was consistent with its low activity and selectivity in photocatalytic CO_2 conversion.

Based on the above discussion, the reaction path of Pt_xCu_{1-x}/Ti catalysts is illustrated in Figure 9. For $Pt_{0.4}Cu_{0.6}$/Ti (Figure 9a), the C atom of the CO_2 molecule adsorbed on the Cu atom, while the O atom did not adsorb onto any atom (A1). Then, H^+ generated from the dissociation of H_2O reacted with the negatively charged CO_2^- to form *COOH (A2). Subsequently, a second dissociated H^+ attacked the OH of *COOH, generating H_2O and *CO where H_2O desorbed from the surface and *CO (A3) remained on the surface. Next, *CO received an additional electron and combined with a third dissociated H^+ to form *CHO (A4). *CHO further underwent hydrogenation, producing H_2O and *C (A5), with H_2O desorbing, and *C remaining on the catalyst surface. Finally, *C underwent four successive electron transfers and hydrogenation with H^+ processes to produce CH_4 (A9). Nevertheless, the reduction of CO_2 on $Pt_{0.5}Cu_{0.5}$/Ti and $Pt_{0.8}Cu_{0.2}$/Ti (Figure 9b,c) began with the adsorption of the C and O atoms of the CO_2 molecule on the Cu and Pt atoms of adjacent Cu−Pt atomic pairs (B1, C1), respectively. Then, these adsorbed atoms received electrons (photoinduced electrons) and combined with H^+ dissociated from H_2O to form the *COOH (B2, C2) configuration. Another H^+ from the dissociation of H_2O attacked the OH of *COOH, forming a water molecule that desorbed from the surface, leaving *CO (B3, C3). Subsequently, *CO received an electron and combined with a third H^+, generating *CHO (B4, C4). Finally, *CHO underwent electron transfer combining with a dissociated H^+ three times to produce CH_4 (B7, C7). This finding provided further insight into the origin of the selectivity differences over Pt_xCu_{1-x}/Ti catalysts.

To better understand the reasons for the changes in the CH_4 selectivity on Pt_xCu_{1-x}/Ti, DFT calculations were performed. The Gibbs free energy diagram indicated that, compared with $Pt_{0.4}Cu_{0.6}$/Ti (0.81 eV) with CO_2 adsorbed in the M-C configuration (Figure 9a), $Pt_{0.5}Cu_{0.5}$/Ti (−0.46 eV) and $Pt_{0.8}Cu_{0.2}$/Ti (0.36 eV) with CO_2 adsorbed in the O-M-M-C configuration (Figure 9b,c) exhibited lower energy barriers for the generation of *COOH from $*CO_2$, suggesting significantly enhanced kinetics of the initial step of CO_2 reduction. This finding was consistent with the results of charge density difference calculations. Furthermore, the Gibbs free energy of $Pt_{0.8}Cu_{0.2}$/Ti required for step $*CO + H^+ + e^- \rightarrow *CHO$ was

https://doi.org/10.1021/acsami.4c03861
ACS Appl. Mater. Interfaces 2024, 16, 22089−22101

much higher than that of $Pt_{0.5}Cu_{0.5}$/Ti. In other words, *CO species had difficulty accepting additional electrons and reacting with H^+ to form *CHO and preferred to desorb as gaseous CO. This was the reason for the lower CH_4 selectivity observed in $Pt_{0.8}Cu_{0.2}$/Ti. Moreover, the formation of $*CH_3O$ and the subsequent generation of gaseous CH_4 were kinetically favorable on $Pt_{0.5}Cu_{0.5}$/Ti, which required a much lower free energy compared with $Pt_{0.8}Cu_{0.2}$/Ti, leading to its higher CH_4 production. These results further confirm the crucial role of adsorption modes in determining the reaction pathways and selectivity of the photocatalytic CO_2 reduction process on the Pt_xCu_{1-x}/Ti catalysts.

4. CONCLUSIONS

In this work, the coordination environments of Pt and Cu in Pt_xCu_{1-x} alloy catalysts supported on TiO_2 were fine-tuned by simply regulating the ratios of Pt to Cu. Based on comprehensive structural characterization results and DFT calculations, it was found that Pt_xCu_{1-x} catalysts with different local coordination environments could be obtained on TiO_2 supports. The difference in the local coordination environments of the Pt_xCu_{1-x} species not only impacted the efficiency of charge carrier separation but also significantly influenced the CO_2 adsorption mode. In detail, compared with the M-C adsorption configuration of $Pt_{0.4}Cu_{0.6}$/Ti, $Pt_{0.5}Cu_{0.5}$/Ti exhibited stronger adsorption with the O-M-M-C configuration, which facilitated more electron transfer along the C−M and M−O bonds and resulted in enhancement of catalytic activity. Further analysis demonstrated that catalysts with different Pt/Cu ratios followed different reaction pathways due to different CO_2 adsorption modes, resulting in significant differences in both activity and selectivity. $Pt_{0.5}Cu_{0.5}$/Ti catalyst exhibited a larger number of activated *CHO species, indicating the occurrence of photocatalytic CO_2 reduction via the "formaldehyde" pathway. These findings are expected to inspire new insights for the design of novel alloy photocatalysts with excellent CO_2 reduction activity from the perspective of surface coordination environment engineering.

■ ASSOCIATED CONTENT

Supporting Information

The Supporting Information is available free of charge at https://pubs.acs.org/doi/10.1021/acsami.4c03861.

Comparison of photocatalytic CO_2 reduction performance, external quantum efficiency, integral area of peaks in CO_2-TPD profiles, schematic illustration for preparation, TEM images, XRD, N_2 physisorption results, XPS, GC-MS, chromatogram profile, ATR-FTIR, Raman spectra, UV−vis spectra, equivalent circuit diagram, PL spectra, and *in situ* ESR (PDF)

■ AUTHOR INFORMATION

Corresponding Author

Haiqin Wan − *State Key Laboratory of Pollution Control and Resource Reuse, School of the Environment, Nanjing University, Nanjing 210023, PR China;* orcid.org/0000-0003-0639-4576; Email: wanhq@nju.edu.cn

Authors

Xin Wang − *State Key Laboratory of Pollution Control and Resource Reuse, School of the Environment, Nanjing University, Nanjing 210023, PR China*

Haohong Liao − *State Key Laboratory of Mesoscopic Chemistry of MOE, School of Chemistry and Chemical Engineering, Nanjing University, Nanjing 210023, PR China*

Wei Tan − *State Key Laboratory of Pollution Control and Resource Reuse, School of the Environment, Nanjing University, Nanjing 210023, PR China;* orcid.org/0000-0002-1481-9346

Wang Song − *State Key Laboratory of Mesoscopic Chemistry of MOE, School of Chemistry and Chemical Engineering, Nanjing University, Nanjing 210023, PR China*

Xue Li − *State Key Laboratory of Pollution Control and Resource Reuse, School of the Environment, Nanjing University, Nanjing 210023, PR China*

Jiawei Ji − *State Key Laboratory of Mesoscopic Chemistry of MOE, School of Chemistry and Chemical Engineering, Nanjing University, Nanjing 210023, PR China*

Xiaoqian Wei − *State Key Laboratory of Pollution Control and Resource Reuse, School of the Environment, Nanjing University, Nanjing 210023, PR China*

Cong Wu − *State Key Laboratory of Pollution Control and Resource Reuse, School of the Environment, Nanjing University, Nanjing 210023, PR China*

Chenxu Yin − *State Key Laboratory of Pollution Control and Resource Reuse, School of the Environment, Nanjing University, Nanjing 210023, PR China*

Qing Tong − *Jiangsu Key Laboratory of Vehicle Emissions Control, Center of Modern Analysis, Nanjing University, Nanjing 210023, PR China*

Bo Peng − *SINOPEC Research Institute of Petroleum Processing Co., Ltd., Beijing 100083, China*

Shangcong Sun − *SINOPEC Research Institute of Petroleum Processing Co., Ltd., Beijing 100083, China*

Lin Dong − *State Key Laboratory of Pollution Control and Resource Reuse, School of the Environment and Jiangsu Key Laboratory of Vehicle Emissions Control, Center of Modern Analysis, Nanjing University, Nanjing 210023, PR China;* orcid.org/0000-0002-8393-6669

Complete contact information is available at: https://pubs.acs.org/10.1021/acsami.4c03861

Notes

The authors declare no competing financial interest.

■ ACKNOWLEDGMENTS

This work was supported by State Key Laboratory of Catalytic Materials and Reaction Engineering (RIPP, SINOPEC), the National Natural Science Foundation of China (Nos. 21976082, 22106067, and 22272077).

■ REFERENCES

(1) Huang, H.; Shi, R.; Li, Z.; Zhao, J.; Su, C.; Zhang, T. Triphase Photocatalytic CO_2 Reduction over Silver-Decorated Titanium Oxide at a Gas−Water Boundary. *Angew. Chem.* **2022**, *134* (17), e202200802.

(2) Lei, Q.; Yuan, H.; Du, J.; Ming, M.; Yang, S.; Chen, Y.; Lei, J.; Han, Z. Photocatalytic CO_2 reduction with aminoanthraquinone organic dyes. *Nat. Commun.* **2023**, *14* (1), 1087.

(3) Jia, X.; Hu, C.; Sun, H.; Cao, J.; Lin, H.; Li, X.; Chen, S. A dual defect co-modified S-scheme heterojunction for boosting photocatalytic CO_2 reduction coupled with tetracycline oxidation. *Appl. Catal., B* **2023**, *324*, No. 122232.

(4) Guo, S.-T.; Tang, Z.-Y.; Du, Y.-W.; Liu, T.; Ouyang, T.; Liu, Z.-Q. Chlorine anion stabilized Cu_2O/ZnO photocathode for selective CO_2 reduction to CH_4. *Appl. Catal., B* **2023**, *321*, No. 122035.

(5) Si, S.; Shou, H.; Mao, Y.; Bao, X.; Zhai, G.; Song, K.; Wang, Z.; Wang, P.; Liu, Y.; Zheng, Z.; Dai, Y.; Song, L.; Huang, B.; Cheng, H. Low-Coordination Single Au Atoms on Ultrathin $ZnIn_2S_4$ Nanosheets for Selective Photocatalytic CO_2 Reduction towards CH_4. *Angew. Chem.* **2022**, *134* (41), e202209446.
(6) Tang, Z.; He, W.; Wang, Y.; Wei, Y.; Yu, X.; Xiong, J.; Wang, X.; Zhang, X.; Zhao, Z.; Liu, J. Ternary heterojunction in rGO-coated Ag/Cu_2O catalysts for boosting selective photocatalytic CO_2 reduction into CH_4. *Appl. Catal., B* **2022**, *311*, No. 121371.
(7) Wang, Y.; Chen, E.; Tang, J. Insight on Reaction Pathways of Photocatalytic CO_2 Conversion. *ACS Catal.* **2022**, *12* (12), 7300−7316.
(8) Hu, Y.; Zhan, F.; Wang, Q.; Sun, Y.; Yu, C.; Zhao, X.; Wang, H.; Long, R.; Zhang, G.; Gao, C.; Zhang, W.; Jiang, J.; Tao, Y.; Xiong, Y. Tracking mechanistic pathway of photocatalytic CO_2 reaction at Ni sites using operando, time-resolved spectroscopy. *J. Am. Chem. Soc.* **2020**, *142* (12), 5618−5626.
(9) Lin, X.; Xia, S.; Zhang, L.; Zhang, Y.; Sun, S.; Chen, Y.; Chen, S.; Ding, B.; Yu, J.; Yan, J. Fabrication of flexible mesoporous black Nb_2O_5 nanofiber films for visible-light-driven photocatalytic CO_2 reduction into CH_4. *Adv. Mater.* **2022**, *34* (16), 2200756.
(10) Dumele, O.; Đorđević, L.; Sai, H.; Cotey, T. J.; Sangji, M. H.; Sato, K.; Dannenhoffer, A. J.; Stupp, S. I. Photocatalytic aqueous CO_2 reduction to CO and CH_4 sensitized by ullazine supramolecular polymers. *J. Am. Chem. Soc.* **2022**, *144* (7), 3127−3136.
(11) Sun, Q. M.; Xu, J. J.; Tao, F. F.; Ye, W.; Zhou, C.; He, J. H.; Lu, J. M. Boosted inner surface charge transfer in perovskite nanodots@ mesoporous titania frameworks for efficient and selective photocatalytic CO_2 reduction to methane. *Angew. Chem., Int. Ed. Engl.* **2022**, *61* (20), No. e202200872.
(12) Wang, Z.-W.; Wan, Q.; Shi, Y.-Z.; Wang, H.; Kang, Y.-Y.; Zhu, S.-Y.; Lin, S.; Wu, L. Selective photocatalytic reduction CO_2 to CH_4 on ultrathin TiO_2 nanosheet via coordination activation. *Appl. Catal., B* **2021**, *288*, No. 120000.
(13) Zhang, Y.; Xia, B.; Ran, J.; Davey, K.; Qiao, S. Z. Atomic-level reactive sites for semiconductor-based photocatalytic CO_2 reduction. *Adv. Energy Mater.* **2020**, *10* (9), 1903879.
(14) Madhusudan, P.; Wageh, S.; Al-Ghamdi, A. A.; Zhang, J.; Cheng, B.; Yu, Y. Graphene-$Zn_{0.5}Cd_{0.5}S$ nanocomposite with enhanced visible-light photocatalytic CO_2 reduction activity. *Appl. Surf. Sci.* **2020**, *506*, No. 144683.
(15) Yuan, L.; Qi, M. Y.; Tang, Z. R.; Xu, Y. J. Coupling strategy for CO_2 valorization integrated with organic synthesis by heterogeneous photocatalysis. *Angew. Chem., Int. Ed. Engl.* **2021**, *133* (39), 21320−21342.
(16) Son, H.-J.; Pac, C.; Kang, S. O. Inorganometallic photocatalyst for CO_2 reduction. *Acc. Chem. Res.* **2021**, *54* (24), 4530−4544.
(17) Wang, J.; Guo, R.-t.; Bi, Z.-x.; Chen, X.; Hu, X.; Pan, W.-g. A review on TiO_{2-x}-based materials for photocatalytic CO_2 reduction. *Nanoscale* **2022**, *14*, 11512−11528.
(18) Katal, R.; Masudy-Panah, S.; Tanhaei, M.; Farahani, M. H. D. A.; Jiangyong, H. A review on the synthesis of the various types of anatase TiO_2 facets and their applications for photocatalysis. *Chem. Eng. J.* **2020**, *384*, No. 123384.
(19) Fu, C.; Li, F.; Zhang, J.; Li, D.; Qian, K.; Liu, Y.; Tang, J.; Fan, F.; Zhang, Q.; Gong, X.; Huang, W. Site sensitivity of interfacial charge transfer and photocatalytic efficiency in photocatalysis: methanol oxidation on anatase TiO_2 nanocrystals. *Angew. Chem., Int. Ed.* **2021**, *60* (11), 6160−6169.
(20) Parnicka, P.; Lisowski, W.; Klimczuk, T.; Mikolajczyk, A.; Zaleska-Medynska, A. A novel (Ti/Ce) UiO-X MOFs@ TiO_2 heterojunction for enhanced photocatalytic performance: Boosting via Ce^{4+}/Ce^{3+} and Ti^{4+}/Ti^{3+} redox mediators. *Appl. Catal., B* **2022**, *310*, No. 121349.
(21) Meng, A.; Zhang, L.; Cheng, B.; Yu, J. Dual cocatalysts in TiO_2 photocatalysis. *Adv. Mater.* **2019**, *31* (30), 1807660.
(22) Zhu, S.; Liao, W.; Zhang, M.; Liang, S. Design of spatially separated Au and CoO dual cocatalysts on hollow TiO_2 for enhanced photocatalytic activity towards the reduction of CO_2 to CH_4. *Chem. Eng. J.* **2019**, *361*, 461−469.
(23) Nakaya, Y.; Furukawa, S. Catalysis of Alloys: Classification, Principles, and Design for a Variety of Materials and Reactions. *Chem. Rev.* **2023**, *123* (9), 5859−5947.
(24) Zhou, M.; Li, C.; Fang, J. Noble-Metal Based Random Alloy and Intermetallic Nanocrystals: Syntheses and Applications. *Chem. Rev.* **2021**, *121* (2), 736−795.
(25) Gilroy, K. D.; Ruditskiy, A.; Peng, H.-C.; Qin, D.; Xia, Y. Bimetallic Nanocrystals: Syntheses, Properties, and Applications. *Chem. Rev.* **2016**, *116* (18), 10414−10472.
(26) Cui, X.; Wang, J.; Liu, B.; Ling, S.; Long, R.; Xiong, Y. Turning Au Nanoclusters Catalytically Active for Visible-Light-Driven CO_2 Reduction through Bridging Ligands. *J. Am. Chem. Soc.* **2018**, *140* (48), 16514−16520.
(27) Luo, L.; Duan, Z.; Li, H.; Kim, J.; Henkelman, G.; Crooks, R. M. Tunability of the Adsorbate Binding on Bimetallic Alloy Nanoparticles for the Optimization of Catalytic Hydrogenation. *J. Am. Chem. Soc.* **2017**, *139* (15), 5538−5546.
(28) Kumar, A.; Bui, V. Q.; Lee, J.; Wang, L.; Jadhav, A. R.; Liu, X.; Shao, X.; Liu, Y.; Yu, J.; Hwang, Y.; Bui, H. T. D.; Ajmal, S.; Kim, M. G.; Kim, S. G.; Park, G. S.; Kawazoe, Y.; Lee, H. Moving beyond bimetallic-alloy to single-atom dimer atomic-interface for all-pH hydrogen evolution. *Nat. Commun.* **2021**, *12* (1), 6766.
(29) Long, R.; Li, Y.; Liu, Y.; Chen, S.; Zheng, X.; Gao, C.; He, C.; Chen, N.; Qi, Z.; Song, L.; Jiang, J.; Zhu, J.; Xiong, Y. Isolation of Cu Atoms in Pd Lattice: Forming Highly Selective Sites for Photocatalytic Conversion of CO_2 to CH_4. *J. Am. Chem. Soc.* **2017**, *139* (12), 4486−4492.
(30) Wang, J.; Li, Y.; Zhao, J.; Xiong, Z.; Zhao, Y.; Zhang, J. PtCu alloy cocatalysts for efficient photocatalytic CO_2 reduction into CH_4 with 100% selectivity. *Catal. Sci. & Technol.* **2022**, *12* (11), 3454−3463.
(31) Lee, S.; Jeong, S.; Kim, W. D.; Lee, S.; Lee, K.; Bae, W. K.; Moon, J. H.; Lee, S.; Lee, D. C. Low-coordinated surface atoms of CuPt alloy cocatalysts on TiO_2 for enhanced photocatalytic conversion of CO_2. *Nanoscale* **2016**, *8* (19), 10043−8.
(32) Cheng, L.; Zhang, P.; Wen, Q.; Fan, J.; Xiang, Q. Copper and platinum dual-single-atoms supported on crystalline graphitic carbon nitride for enhanced photocatalytic CO_2 reduction. *Chin. J. Catal.* **2022**, *43* (2), 451−460.
(33) Wong, G. D. H.; Law, W. C.; Tan, F. N.; Gan, W. L.; Ang, C. C. I.; Xu, Z.; Seet, C. S.; Lew, W. S. Thermal behavior of spin-current generation in Pt_xCu_{1-x} devices characterized through spin-torque ferromagnetic resonance. *Sci. Rep.* **2020**, *10* (1), 9631.
(34) Cheng, L.; Li, B.; Yin, H.; Fan, J.; Xiang, Q. Cu clusters immobilized on Cd-defective cadmium sulfide nano-rods towards photocatalytic CO_2 reduction. *J. Mater. Sci. & Technol.* **2022**, *118*, 54−63.
(35) Zhan, P.; Yang, S.; Huang, L.; Zhang, X.; Li, X.; Lu, L.; Qin, P. Synthesis of AuX (X = Ni, Ga, Mo, Zn, and Cr) Alloy Aerogels as High-Performance Electrocatalytic CO_2 Reduction Reaction Catalysts. *Langmuir* **2023**, *39* (23), 8306−8313.
(36) Cheng, L.; Yue, X.; Fan, J.; Xiang, Q. Site-Specific Electron-Driving Observations of CO2-to-CH4 Photoreduction on Co-Doped CeO2/Crystalline Carbon Nitride S-Scheme Heterojunctions. *Adv. Mater.* **2022**, *34* (27), 2200929.
(37) Li, C.; Kwon, S.; Chen, X.; Zhang, L.; Sharma, A.; Jiang, S.; Zhang, H.; Zhou, M.; Pan, J.; Zhou, G.; Goddard, W. A., III; Fang, J. Improving Oxygen Reduction Performance of Surface-Layer-Controlled Pt−Ni Nano-Octahedra via Gaseous Etching. *Nano Lett.* **2023**, *23* (8), 3476−3483.
(38) Li, H.; Gan, K.; Li, R.; Huang, H.; Niu, J.; Chen, Z.; Zhou, J.; Yu, Y.; Qiu, J.; He, X. Highly Dispersed NiO Clusters Induced Electron Delocalization of Ni-N-C Catalysts for Enhanced CO_2 Electroreduction. *Adv. Funct. Mater.* **2023**, *33* (1), 2208622.
(39) Zhang, X.; Song, Y.; Niu, X.; Lin, X.; Zhong, S.; Lin, H.; Teng, B.; Bai, S. Emerging hollow artificial photosynthetic system with S-scheme heterojunction sandwiched between layered redox cocatalysts for

https://doi.org/10.1021/acsami.4c03861
ACS Appl. Mater. Interfaces 2024, 16, 22089−22101

overall CO_2 reduction and H_2O oxidation. *Appl. Catal., B* **2024**, *342*, No. 123445.
(40) Yang, G.; Wang, S.; Wu, Y.; Zhou, H.; Zhao, W.; Zhong, S.; Liu, L.; Bai, S. Spatially Separated Redox Cocatalysts on Ferroelectric Nanoplates for Improved Piezophotocatalytic CO_2 Reduction and H_2O Oxidation. *ACS Appl. Mater. & Interfaces* **2023**, *15* (11), 14228−14239.
(41) Wang, J.-W.; Jiang, L.; Huang, H.-H.; Han, Z.; Ouyang, G. Rapid electron transfer via dynamic coordinative interaction boosts quantum efficiency for photocatalytic CO2 reduction. *Nat. Commun.* **2021**, *12* (1), 4276.
(42) Cheng, Y.-Z.; Ji, W.; Hao, P.-Y.; Qi, X.-H.; Wu, X.; Dou, X.-M.; Bian, X.-Y.; Jiang, D.; Li, F.-T.; Liu, X.-F.; Yang, D.-H.; Ding, X.; Han, B.-H. A Fully Conjugated Covalent Organic Framework with Oxidative and Reductive Sites for Photocatalytic Carbon Dioxide Reduction with Water. *Angew. Chem., Int. Ed.* **2023**, *62* (36), No. e202308523.
(43) Chen, J.; Xiong, S.; Liu, H.; Shi, J.; Mi, J.; Liu, H.; Gong, Z.; Oliviero, L.; Maugé, F.; Li, J. Reverse oxygen spillover triggered by CO adsorption on Sn-doped Pt/TiO_2 for low-temperature CO oxidation. *Nat. Commun.* **2023**, *14* (1), 3477.
(44) Zhang, S. P.; Lin, J. S.; Lin, R. K.; Radjenovic, P. M.; Yang, W. M.; Xu, J.; Dong, J. C.; Yang, Z. L.; Hang, W.; Tian, Z. Q.; Li, J. F. In situ Raman study of the photoinduced behavior of dye molecules on TiO_2(hkl) single crystal surfaces. *Chem. Sci.* **2020**, *11* (25), 6431−6435.
(45) Li, X. l.; Yang, G. q.; Li, S. s.; Xiao, N.; Li, N.; Gao, Y. Q.; Lv, D.; Ge, L. Novel dual co-catalysts decorated Au@HCS@PdS hybrids with spatially separated charge carriers and enhanced photocatalytic hydrogen evolution activity. *Chem. Eng. J.* **2020**, *379*, No. 122350.
(46) Boppella, R.; Yang, W.; Tan, J.; Kwon, H. C.; Park, J.; Moon, J. Black phosphorus supported Ni_2P co-catalyst on graphitic carbon nitride enabling simultaneous boosting charge separation and surface reaction. *Appl. Catal., B* **2019**, *242*, 422−430.
(47) Cai, X.; Zeng, Z.; Liu, Y.; Li, Z.; Gu, X.; Zhao, Y.; Mao, L.; Zhang, J. Visible-light-driven water splitting by yolk-shelled $ZnIn_2S_4$-based heterostructure without noble-metal co-catalyst and sacrificial agent. *Appl. Catal., B* **2021**, *297*, No. 120391.
(48) Yu, Y.; Dong, X. a.; Chen, P.; Geng, Q.; Wang, H.; Li, J.; Zhou, Y.; Dong, F. Synergistic Effect of Cu Single Atoms and Au−Cu Alloy Nanoparticles on TiO_2 for Efficient CO_2 Photoreduction. *ACS Nano* **2021**, *15* (9), 14453−14464.
(49) Cheng, L.; Chen, Q.; Li, J.; Liu, H. Boosting the photocatalytic activity of $CdLa_2S_4$ for hydrogen production using Ti_3C_2 MXene as a co-catalyst. *Appl. Catal., B* **2020**, *267*, No. 118379.
(50) Wang, G.; Huang, R.; Zhang, J.; Mao, J.; Wang, D.; Li, Y. Synergistic Modulation of the Separation of Photo-Generated Carriers via Engineering of Dual Atomic Sites for Promoting Photocatalytic Performance. *Adv. Mater.* **2021**, *33* (52), 2105904.
(51) Kusiak-Nejman, E.; Morawski, A. W. TiO_2/graphene-based nanocomposites for water treatment: A brief overview of charge carrier transfer, antimicrobial and photocatalytic performance. *Appl. Catal., B* **2019**, *253*, 179−186.
(52) Han, Y.; Wu, J.; Li, Y.; Gu, X.; He, T.; Zhao, Y.; Huang, H.; Liu, Y.; Kang, Z. Carbon dots enhance the interface electron transfer and photoelectrochemical kinetics in TiO_2 photoanode. *Appl. Catal., B* **2022**, *304*, No. 120983.
(53) Kreft, S.; Schoch, R.; Schneidewind, J.; Rabeah, J.; Kondratenko, E. V.; Kondratenko, V. A.; Junge, H.; Bauer, M.; Wohlrab, S.; Beller, M. Improving Selectivity and Activity of CO_2 Reduction Photocatalysts with Oxygen. *Chem.* **2019**, *5* (7), 1818−1833.
(54) Villamena, F. A.; Locigno, E. J.; Rockenbauer, A.; Hadad, C. M.; Zweier, J. L. Theoretical and Experimental Studies of the Spin Trapping of Inorganic Radicals by 5,5-Dimethyl-1-Pyrroline N-Oxide (DMPO). 1. Carbon Dioxide Radical Anion. *J. Phys. Chem. A* **2006**, *110* (49), 13253−13258.
(55) Pu, Y.; Luo, Y.; Wei, X.; Sun, J.; Li, L.; Zou, W.; Dong, L. Synergistic effects of Cu_2O-decorated CeO_2 on photocatalytic CO_2 reduction: Surface Lewis acid/base and oxygen defect. *Appl. Catal., B* **2019**, *254*, 580−586.
(56) Wang, Y.; Hu, J.; Ge, T.; Chen, F.; Lu, Y.; Chen, R.; Zhang, H.; Ye, B.; Wang, S.; Zhang, Y.; Ma, T.; Huang, H. Gradient Cationic Vacancies Enabling Inner-to-outer Tandem Homojunction: Strong local Internal Electric Field and Reformed basic sites Boosting CO_2 Photoreduction. *Adv. Mater.* **2023**, 2302538.
(57) Hiragond, C. B.; Biswas, S.; Powar, N. S.; Lee, J.; Gong, E.; Kim, H.; Kim, H. S.; Jung, J.-W.; Cho, C.-H.; Wong, B. M.; In, S.-I. Surface-modified Ag@Ru-P25 for photocatalytic CO_2 conversion with high selectivity over CH_4 formation at the solid−gas interface. *Carbon Energy* **2023**, e386.
(58) Gattrell, M.; Gupta, N.; Co, A. A review of the aqueous electrochemical reduction of CO_2 to hydrocarbons at copper. *Electroanal. Chem.* **2006**, *594* (1), 1−19.
(59) Santiago Rodríguez, Y.; Barreto Rodríguez, E.; Curet Arana, M. C. Quantum mechanical study of CO_2 and CO hydrogenation on Cu(111) surfaces doped with Ga, Mg, and Ti. *J. Mol. Catal. A. Chem.* **2016**, *423*, 319−332.
(60) Rasko, J.; Solymosi, F. Infrared Spectroscopic Study of the Photoinduced Activation of CO_2 on TiO_2 and Rh/TiO_2 Catalysts. *J. Phys. Chem.* **1994**, *98* (29), 7147−7152.
(61) Li, H.; Song, Q.; Wan, S.; Tung, C. W.; Liu, C.; Pan, Y.; Luo, G.; Chen, H. M.; Cao, S.; Yu, J.; Zhang, L. Atomic Interface Engineering of Single-Atom Pt/TiO_2-Ti_3C_2 for Boosting Photocatalytic CO_2 Reduction. *Small* **2023**, *19*, 2301711.
(62) Wang, K.; Qin, H.; Li, J.; Cheng, Q.; Zhu, Y.; Hu, H.; Peng, J.; Chen, S.; Wang, G.; Chou, S.; Dou, S.; Xiao, Y. Metallic $AgInS_2$ nanocrystals with sulfur vacancies boost atmospheric CO_2 photoreduction under near-infrared light illumination. *Appl. Catal., B* **2023**, *332*, No. 122763.
(63) Yin, H.; Dong, F.; Wang, D.; Li, J. Coupling Cu Single Atoms and Phase Junction for Photocatalytic CO_2 Reduction with 100% CO Selectivity. *ACS Catal.* **2022**, *12* (22), 14096−14105.
(64) Xiong, Z.; Xu, Z.; Li, Y.; Dong, L.; Wang, J.; Zhao, J.; Chen, X.; Zhao, Y.; Zhao, H.; Zhang, J. Incorporating highly dispersed and stable Cu^+ into TiO_2 lattice for enhanced photocatalytic CO_2 reduction with water. *Appl. Surf. Sci.* **2020**, *507*, No. 145095.
(65) Lee, I.; Delbecq, F.; Morales, R.; Albiter, M. A.; Zaera, F. Tuning selectivity in catalysis by controlling particle shape. *Nat. Mater.* **2009**, *8* (2), 132−138.
(66) Katayama, Y.; Giordano, L.; Rao, R. R.; Hwang, J.; Muroyama, H.; Matsui, T.; Eguchi, K.; Shao-Horn, Y. Surface (Electro)chemistry of CO_2 on Pt Surface: An in Situ Surface-Enhanced Infrared Absorption Spectroscopy Study. *J. Phys. Chem. C* **2018**, *122* (23), 12341−12349.
(67) Fu, J.; Jiang, K.; Qiu, X.; Yu, J.; Liu, M. Product selectivity of photocatalytic CO_2 reduction reactions. *Mater. Today* **2020**, *32*, 222−243.
(68) Yang, D.; Pei, W.; Zhou, S.; Zhao, J.; Ding, W.; Zhu, Y. Controllable Conversion of CO_2 on Non-Metallic Gold Clusters. *Angew. Chem., Int. Ed.* **2020**, *59* (5), 1919−1924.
(69) Li, X.; Sun, Y.; Xu, J.; Shao, Y.; Wu, J.; Xu, X.; Pan, Y.; Ju, H.; Zhu, J.; Xie, Y. Selective visible-light-driven photocatalytic CO_2 reduction to CH_4 mediated by atomically thin $CuIn_5S_8$ layers. *Nat. Energy* **2019**, *4* (8), 690−699.

https://doi.org/10.1021/acsami.4c03861
ACS Appl. Mater. Interfaces 2024, 16, 22089−22101